Enhanced Low-Temperature Thermoelectric Performance in the Two-Dimensional *A*Mn*X* Family

Xincan Wang,[1] De Zhang,[1] Xu Lu,[1] Guang Han,[2] Xiaolong Yang,[1] Guoyu Wang,[2] Zizhen Zhou,[1,*] Huixia Fu,[1,†] and Xiaoyuan Zhou[1,‡]

[1] *College of Physics and Center of Quantum Materials and Devices, Chongqing University, Chongqing 401331, China*

[2] *College of Materials Science and Engineering, Chongqing University, Chongqing 400044, China*

(Received 20 March 2023; revised 8 June 2023; accepted 30 June 2023; published 24 July 2023)

Thermoelectric (TE) coolers show considerable promise for replacing aging refrigeration devices, which suffer from the poor low-temperature performance of most TE materials due to the small entropy of carriers and weak lattice vibrational anharmonicity. Here we propose that two-dimensional (2D) semiconductors with multiple bonding layers can be potential TE cooling materials, and the 2D AMnX ($A = \mathrm{Sr, Ba}$; $X = \mathrm{Sn, Pb}$) family is identified as an example. Owing to the d-orbital inversion of the Mn element, both the valence and conduction bands possess continuously square-shaped band edges with slight energy divergence, which trigger high mobility and sharply enhanced density of states near the Fermi level, thereby producing large power factors for both p- and n- type materials. Moreover, the coexistence of soft covalent bonds and ionic layers lowers phonon group velocity and strengthens phonon scattering, resulting in extremely low lattice thermal conductivity. At optimal carrier concentrations, both p- and n-type SrMnPb quintuple layers can reach ultrahigh room-temperature ZT above 2.0, with excellent average ZT beyond 1.8 from 150 to 350 K. This work not only proposes a tellurium-free alternative for TE refrigeration, but also provides general indicators for guiding the search for high-performance TE cooling materials.

DOI: 10.1103/PhysRevApplied.20.014052

I. INTRODUCTION

Current refrigeration devices account for around 20% of global electricity consumption and the adopted refrigerants usually contain extremely potent greenhouse gases [1,2], thus there are urgent demands for the development of advanced cooling technologies. Thermoelectric (TE) cooling devices, capable of solid-state refrigeration based on the Peltier effect, are among the most promising alternatives owing to the advantages of environmental friendliness, reliability, compactness, silence, and precise temperature control [3–5]. The cooling efficiency of a TE device largely relies on the performance of the material used, which is governed by the dimensionless figure of merit $ZT = S^2\sigma T/\kappa$ (S, Seebeck coefficient; σ, electrical conductivity; T, absolute temperature; κ, total thermal conductivity consisting of electronic κ_e and phonon κ_l counterparts). In contrast to the significant progress made in medium-to-high temperature TE materials [6–10], fewer investigations have focused on improving the low-temperature TE performance of materials for refrigeration. To date, Bi_2Te_3-based alloys developed in the 1950s are still the best room-temperature TE materials [11], although the scarcity of tellurium restricts their wide-scale application. It is thus essential to develop tellurium-free candidates with excellent TE performance near and below room temperature.

TE materials usually exhibit relatively poor performance below room temperature, for two reasons: (i) low S due to the small entropy of carriers; (ii) high κ_l because of weak lattice vibrational scattering. Hicks and Dresselhaus [12] proposed that the quantum size effect in low-dimensional systems could yield a remarkable change in the density of states (DOS) and thereby significantly improve the S [13]. Indeed, many two-dimensional (2D) semiconductors were predicted to hold promising TE performance [14–16], and some of them have been synthesized experimentally, such as monolayer transition metal sulfides [17] and SnSe nanosheets [18]. However, until now, the study of 2D materials for TE refrigeration has been rare because of the high κ_l at low temperature. It has been recognized that 2D films with multiple bonding layers can yield all-scale phonon scattering, resulting in low κ_l even below room temperature. For instance, κ_l is dramatically suppressed in Bi_2Te_3/Sb_2Te_3 superlattice film by the acoustic mismatch between the two components,

*zzzhou@cqu.edu.cn
†hxfu@cqu.edu.cn
‡xiaoyuan2013@cqu.edu.cn

giving rise to a high ZT of 2.4 at 300 K [19]. The intercalation of the Bi monolayer in Bi_2Te_3-based films can import localized vibrations to scatter all-scale phonons, which greatly lowers the κ_l and improves the TE performance near room temperature [14]. In this case, searching for Te-free 2D semiconductors with multiple bonding layers is highly desired for TE refrigeration.

Based on this screening principle, the low-temperature (150–350 K) TE properties of 2D AMnX ($A = \mathrm{Sr, Ba}$; $X = \mathrm{Sn, Pb}$) quintuple layers (QLs) are studied using first-principles calculations. This new class of 2D compounds has recently been predicted to be magnetic topological insulators with multiple bonding layers in primitive cells [20]. Owing to the spin-orbital-coupling- (SOC) induced Mn d band inversion, AMnX QLs show square-shaped band edges for both valence and conduction bands. Such distinctive topological electronic structures promote carrier mobility and sharply enhance the DOS around band edges, giving rise to an extraordinary power factor ($S^2\sigma$) in all the compounds. In addition, it is found that the intrinsic lattice thermal conductivity of SrMnPb is extremely low due to low phonon group velocity and strong phonon scattering, which stem from the large lattice vibrational anharmonicity provoked by the coexistence of weak covalent and ionic bonds. Consequently, a high average figure of merit (ZT_{ave}) approaching 2.0 is found in both p- and n-type SrMnPb, which is superior to those of typical low-temperature TE materials. Combined with good flexibility, the 2D SrMnPb QL can be a promising candidate for application in TE refrigeration in electronic and wearable devices.

II. COMPUTATIONAL DETAILS

The electronic properties of AMnX QLs were calculated based on density functional theory (DFT) [21], as implemented in the Vienna *ab initio* simulation package [22]. The exchange correlation potential of Perdew, Burke, and Ernzerhof (PBE) within the generalized gradient approximation (GGA) was adopted [23,24]. The projector-augmented-wave method and SOC were considered in the calculation. The QL structure was modeled by adopting a vacuum distance of 25 Å to eliminate the periodic images. A $30 \times 30 \times 1$ k-point grid was used for Brillouin zone (BZ) sampling. The residual force of the calculated cell was set to 0.01 eV Å^{-1} and the energy convergence threshold was $10-^{7}$ eV. Meanwhile, the cutoff energy of 500 eV was adopted. The GGA + U method was chosen to describe the localized d orbitals of Mn, in which the U was used to describe the Coulomb interaction among electrons living in the localized orbitals [25–28]. $U = 3$ eV was finally adopted since the calculated lattice parameters of bulk SrMnSn exhibited good agreement with those reported in experimental work [29], and this value has also been adopted for the Mn atom in many other theoretical works [30,31]. The crystal orbital Hamiltonian population (COHP) was calculated using the LOBSTER code.

The electronic transport properties can be calculated by solving the Boltzmann transport equations within the rigid-band model and relaxation-time (τ) approximation, as implemented in the BOLTZTRAP code [32]. Boltzmann transport theory combined with deformation-potential theory has been successfully utilized to predict the electronic transport properties of some 2D materials [33–35]. The electrical conductivity, Seebeck coefficient, and electronic thermal conductivity can be given by

$$\sigma(T,\mu) = e^2 \int_{-\infty}^{+\infty} d\varepsilon \left[-\frac{\partial f(T,\mu,\varepsilon)}{\partial \varepsilon} \right] \sum(\varepsilon), \tag{1}$$

$$S(T,\mu) = \frac{e}{T\sigma(T,\mu)} \int_{-\infty}^{+\infty} d\varepsilon \left[-\frac{\partial f(T,\mu,\varepsilon)}{\partial \varepsilon} \right] \times \sum(\varepsilon)(\varepsilon - \mu), \tag{2}$$

$$\kappa_e(T,\mu) = \frac{e^2}{T} \int_{-\infty}^{+\infty} d\varepsilon \left[-\frac{\partial f(T,\mu,\varepsilon)}{\partial \varepsilon} \right] \times \sum(\varepsilon)(\varepsilon - \mu)^2 - TS^2(T,\mu)\sigma(T,\mu), \tag{3}$$

where μ is chemical potential, e is electron charge, f is Fermi-Dirac distribution function of carriers, and $\sum(\varepsilon)$ is the transport distribution function and defined as

$$\Sigma(\varepsilon) = \frac{1}{\Omega N_k} \sum_{nk} \tau_{nk}^{e} |v_{nk}|^2 \delta(\varepsilon - \varepsilon_{nk}). \tag{4}$$

Here v is electronic group velocity. The temperature-dependent relaxation time τ was given by deformation-potential theory [36] considering the dominance of acoustic phonon scattering,

$$\tau = \frac{\hbar^3 C_{2\mathrm{D}}}{k_B T m^* E^2}. \tag{5}$$

The parameters $\hbar$, $C_{2\mathrm{D}}$, k_B, m^*, and E are Planck's constant, the 2D modulus of elasticity, Boltzmann constant, the effective mass, and the deformation-potential constant, respectively. For the AMnX QL with noncentrosymmetric lattice, the polar optical phonon scattering was also considered [37,38]. Our calculated results imply that the polar optical phonon–induced average carrier scattering rate is nearly 2 orders of magnitude lower than that dominated by acoustic phonons. Therefore, the polar optical phonon scattering can be ignored for the estimation of carrier relaxation time of the AMnX QL. Besides, the calculated band structures and electronic transport properties were also checked using the NANODCAL code [39].

The lattice thermal conductivity was calculated by solving phonon Boltzmann transport equation [40],

$$\kappa_l = \frac{1}{N_q V k_B T^2} \sum_{\lambda} (\hbar\omega_\lambda)^2 v_\lambda^2 \tau_\lambda n_\lambda (n_\lambda + 1), \qquad (6)$$

where N_q is number of q points in the first Brillouin zone, ω_λ is frequency of phonon mode, v_λ is the group velocity of the phonon mode, and τ_λ is phonon lifetime. Based on a $3 \times 3 \times 1$ supercell, the second- and third-order interatomic force constants were given by the PHONOPY package and THIRDORDER.PY script, respectively [41]. A cutoff radius of 0.6 nm was adopted. The lattice thermal conductivity was calculated using the SHENGBTE package [42], and a $51 \times 51 \times 1$ q mesh was adopted for convergent results (see Fig. S1 for convergence test in the Supplemental Material [28]).

III. RESULTS AND DISCUSSION

A. Crystal structure

Figure 1(a) plots the QL structure stacked along the z axis of bulk AMnX, which crystallizes in a tetragonal lattice with space group $P4/nmm$ and has already been experimentally synthesized [29]. Owing to the small interlayer binding energy [20], AMnX QLs can be easily exfoliated from their layered bulk counterparts, with the side view, top view, and 2D BZ shown in Figs. 1(b)–1(d), respectively. The calculated magnetic moments on each Mn atom in the middle of the QL are about $5\mu_B$, resulting in intrinsic antiferromagnetic (AFM) states for AMnX QLs. The AFM configuration remains the lowest energy in all the AMnX QLs (see Table S1 in the Supplemental Material [28]). The Néel temperatures of SrMnPb, SrMnSn, BaMnPb, and BaMnSn are predicted to be 340, 290, 260, and 210 K, respectively [20]. The optimized lattice constants are in good agreement with those reported in previous work [20].

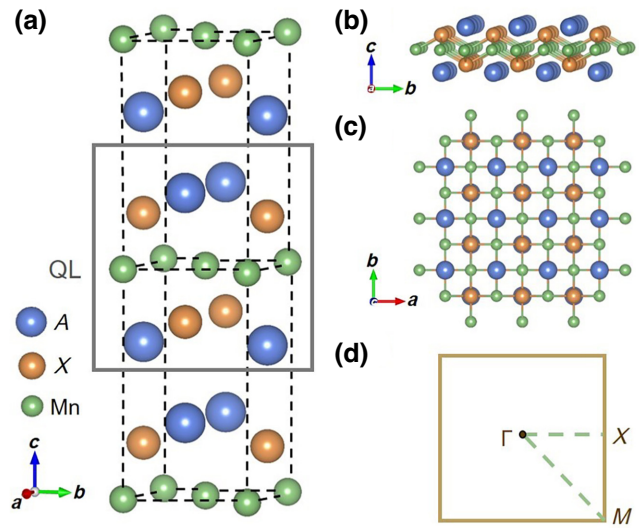

FIG. 1. (a) Crystal structure of bulk AMnX (b) The side view, (c) top view, and (d) 2D BZ of AMnX QL.

It is found that the outer-layer alkaline-earth-metal ions are weakly related to the Mn-X layers. In the SrMnPb QL, the Sr—Pb bond length is 3.462 Å, which is larger than that of the Mn—Pb bond (2.742 Å), indicating that the Sr—Pb bond is relatively weak, thus facilitating low lattice thermal conductivity.

To deeply understand the bond properties, the calculated DOS and COHP of the SrMnPb QL are given in Fig. 2(a). The inset illustrations reflect the COHPs of Mn—Pb, Pb—Sr, and Mn—Sr bonding interactions around an energy range of −10 to 5 eV. To be clear, it should be noted that currently LOBSTER cannot handle the wave function of the SOC, so Fig. 2(a) shows the result without considering SOC. As shown in Fig. S2 in the Supplemental Material [28], the DOS below and above the

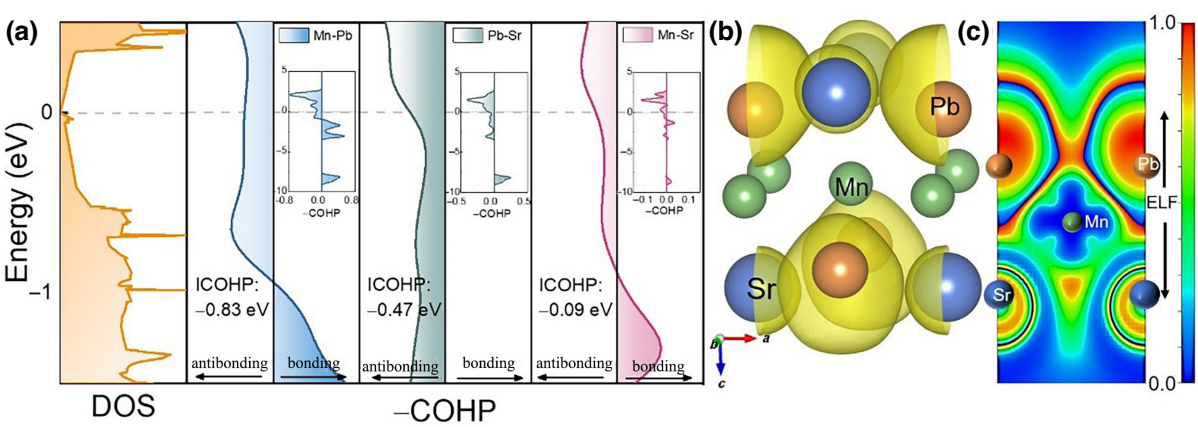

FIG. 2. (a) Calculated density of states (DOS) and crystal orbital Hamilton population (COHP) projected on Mn—Pb, Pb—Sr, and Mn—Sr bonds. (b) Electronic localization function (ELF) of SrMnPb. The ELF value of the isosurface is 0.6. (c) The 2D display of electrostatic potential along the (010) plane of SrMnPb.

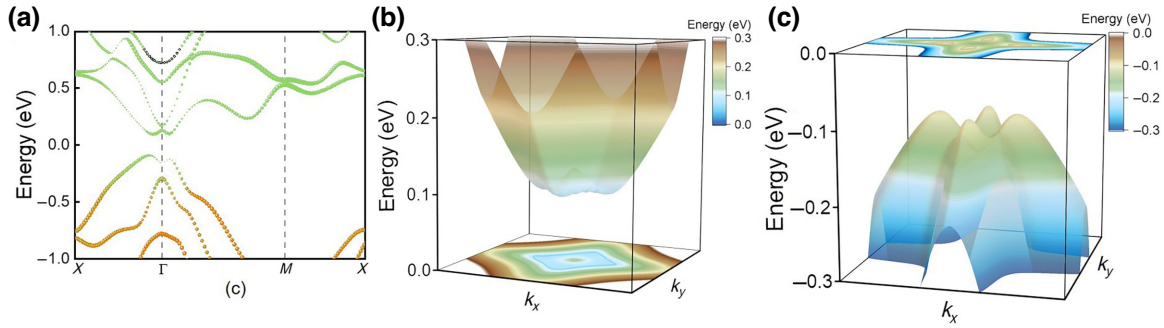

FIG. 3. (a) Orbital decomposed band structures of SrMnPb. The black, green, and orange balls represent the *d* orbital of the Sr atom, the *d* orbital of the Mn atom, and the *p* orbital of the Pb atom, respectively. The 3D morphology of the (b) valence band and (c) conduction band in momentum space.

Fermi level are mainly contributed by Pb *p* orbitals and Mn *d* orbitals, respectively. The DOS of SrMnPb shows a small sharp peak around the Fermi level, and the variation trend of DOS is basically consistent with the COHP. COHPs are essentially pairwise contributions to an effective one-particle energy, while their integral up to the Fermi level is a measure of the bond strength [43]. In order to understand the bonding strength, the integration of orbital Hamilton populations (–ICOHP) was calculated, and the –ICOHP of Mn—Pb, Sr—Pb, and Mn—Sr bonds were found to be 0.83, 0.47, and 0.09 eV, respectively. In terms of bond strength, obviously Mn—Pb bonds are the strongest and most stable, followed by Sr—Pb bonds, and Mn—Sr bonds are the weakest and almost negligible. Both the Mn—Pb and Sr—Pb bonds exhibit relatively low –ICOHP (<1 eV) [44] and antibonding states below the Fermi level, indicating the weak interactions and thus strong lattice anharmonicity. To further figure out the bonding situation in SrMnPb, we calculated its electronic localization function (ELF) with values ranging from 0 to 1. ELF = 0 and ELF = 1 correspond to perfect localization and total delocalization, respectively, and ELF = 0.5 corresponds to the electron gas. Figures 2(b) and 2(c) show the three-dimensional (3D) and projected 2D [in the (010) plane] ELF of the SrMnPb QL at 0 GPa, respectively. In Fig. 3(b), the water-drop ELF surrounds Pb atoms, and a spherical ELF surrounds Sr atoms. The strong electron localization also reflects the weakened bonding nature. Specifically, in Fig. 3(c), the ELF values are close to 1 around Pb and Sr sites but assumed to be negligible surrounding Mn sites, showing a covalent feature of Mn—Pb bonding and an ionic feature of Sr—Pb bonding [45,46].

B. Electronic structure

Given the AFM ground state, the electronic band structures of *A*Mn*X* QLs were calculated by DFT + PBE + *U*, with the results of SrMnPb shown in Fig. 3(a). In the absence of SOC, the band structures are gapless at the Γ point and behave like metal, as shown in Fig. S3 in the Supplemental Material [28]. When considering SOC, a *d*-*d* band inversion contributed by Mn atoms occurs at the Γ point, opening a band gap of 186 meV as displayed in Fig. 3(a), which confirms the magnetic topological phase. The narrow band gap close to that of Bi_2Te_3 implies better TE performance at low-temperature. Figures 3(b) and 3(c) show the 3D morphology of the valence band and conduction band in momentum space, respectively. Induced by *d*-*d* band inversion, both the valence and conduction bands possess a significant feature of saddle-like dispersions, which simply seem to be two band extremes along the Γ-*X* and Γ-*M* directions. From a 3D perspective, the successive band edges are found to form a square-shaped ring with the energy deviation lower than 0.1 eV for both the valence and conduction bands. Such a distinctive band feature is favorable for electrical performance for two reasons: (i) the localized *d* orbital and 2D crystal character lead to continuous band edges with a narrow energy window near the Fermi level, which provides a sharp increase in DOS for high Seebeck coefficient; (ii) SOC-induced topological band inversion triggers energy fluctuation near band edges, leading to small effective mass (about 0.4 m_e for valence band maximum (VBM) and conduction band minimum (CBM) in the SrMnPb QL) guaranteeing high carrier mobility. Note that a similar case is observed in all *A*Mn*X* QLs, which implies large power factors for both *p*- and *n*-type materials in this family.

C. Transport properties

Figure 4 plots the S, σ, and $S^2\sigma$ of *p*- and *n*-type SrMnPb QLs with respect to the carrier concentration in the temperature range of 150 to 350 K. At each temperature, S decreases and σ increases with the rising carrier concentration at relatively high doping levels, leading to an optimal value for a peak power factor. For both *p*- and *n*-type SrMnPb QLs, the Seebeck coefficients at optimal carrier concentrations are above 200 V K^{-1} in the investigated temperature region, benefiting from

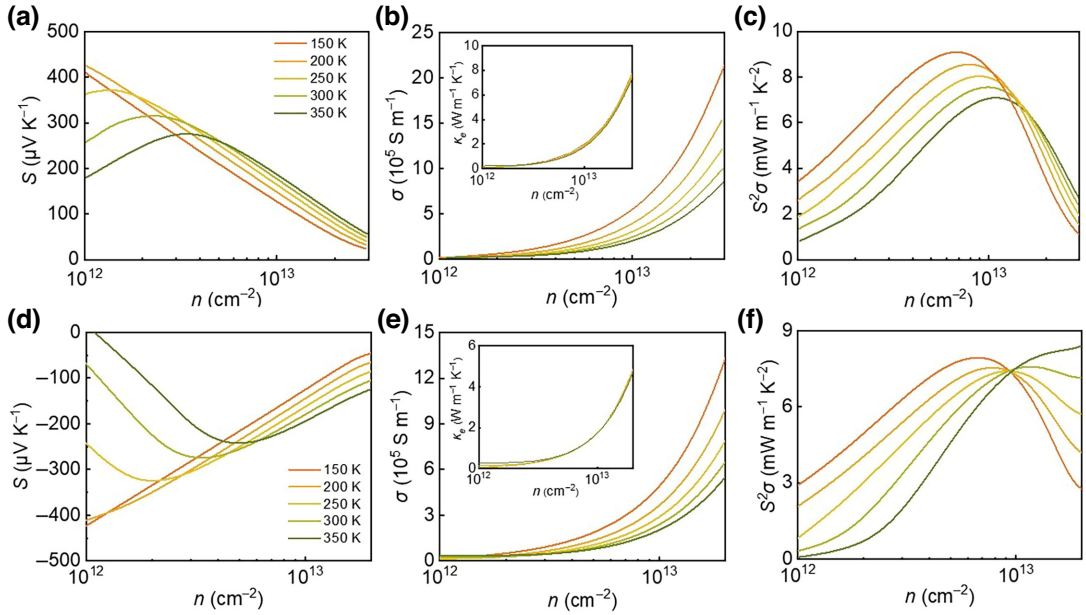

FIG. 4. (a) Seebeck coefficient, (b) conductivity, and (c) power factor as a function of carrier concentration for p-type SrMnPb QL. (d) Seebeck coefficient, (e) conductivity, and (f) power factor as a function of carrier concentration for n-type SrMnPb QL. The insets in (b),(e) are the p- and n-type electronic thermal conductivity, respectively.

the strong energy-dependent DOS produced by successive band edges. Figures 4(b) and 4(e) depict the p- and n-type σ, respectively, with the corresponding electronic thermal conductivity ($\kappa_e = L\sigma T$, where L is the Lorentz constant) plotted in the insets. The room-temperature σ exceeds 10^5 S m^{-1} at the carrier concentration of around 10^{13} cm^{-2}, which stems from the high mobility above 400 cm^2 V^{-1} s^{-1} governed by small effective mass and weak electron-phonon coupling (E_{DP}) as listed in Table I. Accordingly, the SrMnPb QL exhibits high power factors as shown in Figs. 4(c) and 4(f). At the optimal carrier concentrations, both the p- and n-type room-temperature values reach 6 mW m^{-1} K^{-1}, much larger than those reported in SnSe- and Bi_2Te_3-based 2D systems [47–53], suggesting an excellent TE conversion capability.

TABLE I. Lattice parameters a and c, band gap E_g, deformation-potential constant E_{DP}, effective mass m^*, relaxation time τ, and mobility μ of AMnX materials. Here the c parameter means the height of the quintuple layer in the unit cell for each 2D AMnX system.

		SrMnPb	SrMnSn	BaMnPb	BaMnSn
a (Å)		4.71	4.62	4.89	4.82
c (Å)		5.19	5.24	5.41	5.46
E_g (meV)		186	76.4	49.2	29.3
E_{DP} (eV)	p-type	−6.74	−4.91	−5.68	−4.72
	n-type	−5.47	−5.81	−5.65	−4.49
m^* (m_e)	p-type	0.42	0.28	0.14	0.11
	n-type	0.40	0.25	0.10	0.10
τ (ps)	p-type	0.10	0.33	0.42	0.83
	n-type	0.17	0.26	0.59	0.93
μ (10^3 cm^2 V^{-1} s^{-1})	p-type	0.42	2.10	5.13	13.24
	n-type	0.73	1.83	10.07	15.02

The extraordinary power factor originating from the warped topological band structures can be expanded to other AMnX QLs, which all hold AFM states and have been predicted to be magnetic topological insulators with narrow band gap below 0.2 eV as listed in Table I [20]. As can be seen from Figs. S6–S8 in the Supplemental Material [28], their electronic transport properties exhibit trends similar to those of the SrMnPb QL. It was found that all the AMnX QLs possess large and comparable power factors. In particular, BaMnSn QLs have the lowest effective mass and thereby the highest carrier mobility. This leads to a peak p-type power factor above 40 mW m^{-1} K^{-2} at 150 K, implying its great low-temperature TE potential.

D. Phonon properties

Figure 5(a) illustrates the phonon dispersions and partial phonon DOS (PDOS) of the SrMnPb QL. There are six atoms in a primitive cell resulting in 18 phonon branches, which all have positive frequencies in the BZ, indicating good dynamic stability of the single QL. The acoustic phonons with frequency below 1.5 THz, which usually dominate the lattice thermal transport in a solid, are mainly contributed by Pb and Mn atoms. This is consistent with the fact the Sr cations are weakly bonded with Mn-Pb layers and thereby make minor contributions to phonon heat transport. Owing to the bunched acoustic branches

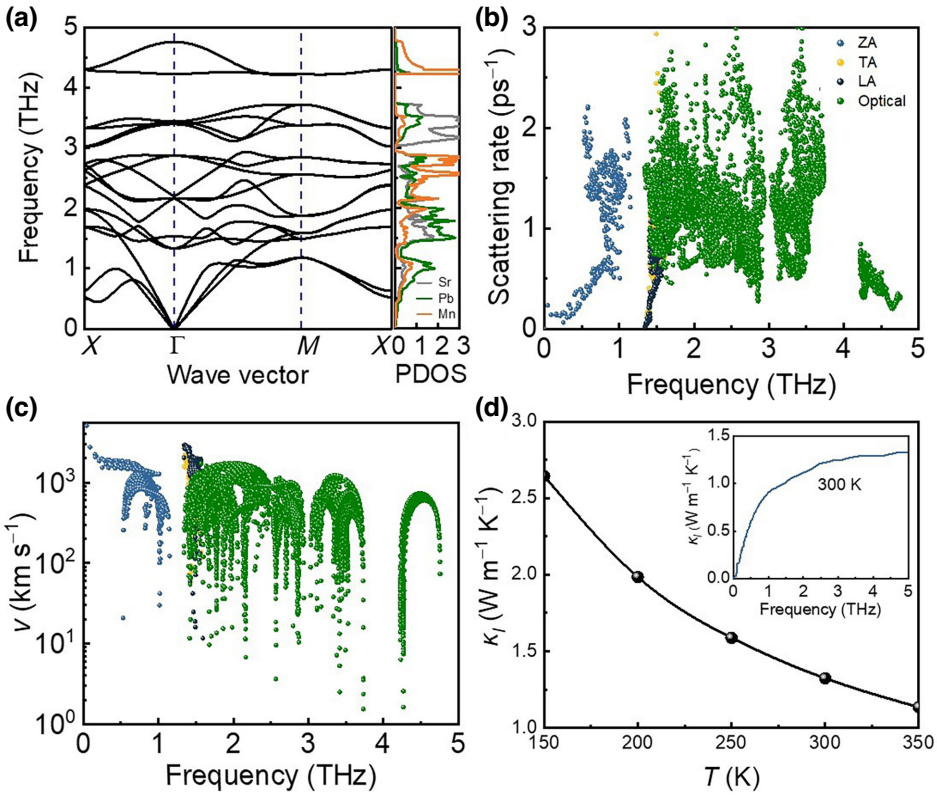

FIG. 5. (a) Phonon dispersions and corresponding PDOS of the SrMnPb QL. (b) Phonon scattering rate of acoustic (ZA, TA, LA) and optical phonon and (c) phonon group velocity as a function of frequency. (d) Temperature-dependent lattice thermal conductivity of SrMnPb QL. The lattice thermal conductivity has been renormalized to compare with those of bulk SrMnPb. The inset shows the cumulative lattice thermal conductivity as a function of phonon frequency.

in the vicinity of the BZ center, low-frequency phonons (<0.5 THz) were found to have small three-phonon scattering rates as shown in Fig. 5(b). With elevated frequency, the scattering rates of acoustic phonons are profoundly intensified because of the interactions with low-frequency optical phonons, suggesting the possibility of low κ_l. The large phonon scattering in the SrMnPb QL is attributed to its strong lattice vibrational anharmonicity as quantified by the Grüneisen parameter in Fig. S9 in the Supplemental Material [28]. The values of the Grüneisen parameter for acoustic phonons can reach 20 in the low-frequency region, which is caused by the intense lattice vibrations of Mn atoms as shown in Fig. S10 in the Supplemental Material [28]. This is caused by the low atomic mass of Mn and weak bonding strength of Mn—Pb bonds reflected by the ELF calculations. For the high-frequency phonons (>1.5 THz) that are dominated by Sr and Pb atoms, the scattering rates are profoundly enhanced, which should be attributed to the isolated Sr atoms acting as rattlers to suppress the phonon transport. Therefore, the large phonon scattering in the SrMnPb QL originates from the coexistence of weak covalent and ionic bonds that induce strong anharmonicity for both low- and high-frequency phonons.

Another important feature in the phonon dispersions of SrMnPb QL is the low cutoff frequency of acoustic phonons, which implies small phonon group velocities. As plotted in Fig. 5(c), almost all the heat-carrying acoustic phonons have group velocities less than 2000 m s^{-1}, which are similar to the cases in typical TE materials with intrinsically low thermal conductivity [54–56] and suggest the weak Mn—Pb bonding feature. Other high-frequency modes show lower group velocities owing to their weaker dispersions, which thereby have minor contributions to the heat transport. Indeed, it is seen from the inset of Fig. 5(d) that more than 70% of κ_l is contributed by low-frequency phonons (<1 THz). Given the strong anharmonic scattering and low phonon group velocity, the SrMnPb QL exhibits ultralow κ_l as presented in Fig. 5(d). By renormalizing the value to compare with those of bulk systems, it can be seen that the room-temperature κ_l of 1.3 W m^{-1} K^{-1} is lower than that of Bi_2Te_3 [47,57]. Even at 150 K, the κ_l is still as low as 2.6 W m^{-1} K^{-1}, making the SrMnPb QL stand out among many other 2D materials for low-temperature TE applications.

E. High *ZT* values

With all the electronic and phonon transport coefficients available, the *ZT* values of the SrMnPb QL could be evaluated as presented in Fig. 6. For both *p*- and *n*-type systems, the highest *ZT* values were attained at 300 K, with the values of 2.3 and 2.0, respectively. The optimized hole and electron concentrations of SrMnPb QL were 2×10^{12} cm^{-2} and 3×10^{12} cm^{-2}, respectively. Considering K and Bi as dopants, we found that SrMnPb QL with stoichiometry of $Sr_{0.9975}K_{0.0025}MnPb$ and $SrMnPb_{0.9955}Bi_{0.0045}$ could realize the optimal hole and electron concentration, respectively. The room-temperature *ZT* of the SrMnPb QL is much

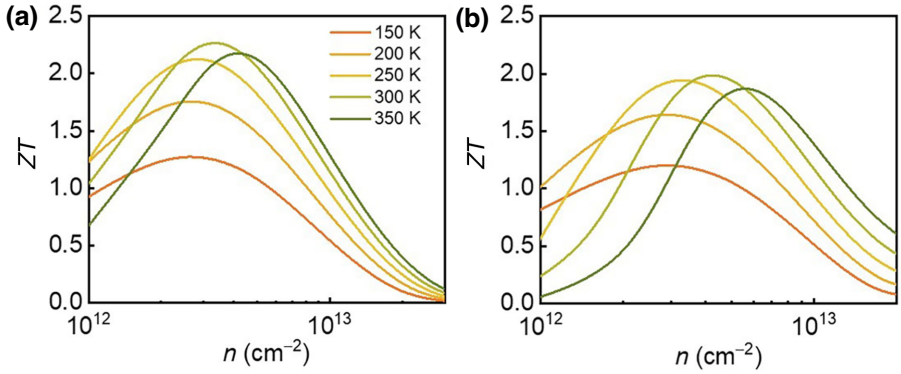

FIG. 6. Figure of merit ZT as a function of carrier concentration for (a) p- and (b) n-type SrMnPb at 150–350 K.

higher than those of current low-temperature TE materials [19,58–61]. More importantly, the ZT values exceed 1.2 in the whole temperature region, giving rise to similar and ultrahigh p- and n-type ZT_{ave} (150–350 K) of 2.0 and 1.8, respectively, which are very desirable for fabrication of TE modules with comparable performance. In addition, considering its lower Young's modulus (around 50 GPa, as shown in Table S2 in the Supplemental Material [28]) compared to those of MoS_2 [62] and graphene [63], 2D SrMnPb may be a favorable candidate for TE refrigeration in microelectronics and wearable devices.

IV. CONCLUSION

In summary, we theoretically uncover the excellent low-temperature TE performance of 2D SrMnPb QL, which shows simultaneously high p- and n-type ZT_{ave} approaching 2.0 (150–350 K) owing to ultralow κ_l and large power factors. The ultralow κ_l originates from the low phonon group velocity and strong lattice vibrational anharmonicity induced by the coexistence of weak covalent and ionic bonds. The large power factors are primarily ascribed to the topological electronic structures with continuous square-like band edges that provoke steeply increased DOS and high carrier mobility. These findings have been extended to other AMnX systems with similar band features, offering an indicator in the discovery of advanced TE materials for refrigeration technologies.

ACKNOWLEDGMENTS

The authors are grateful for financial support from the National Natural Science Foundation of China (Grants No. 52125103, No. 52071041, No. 12104072, No. 12004254, and No. 12104071), the Venture and Innovation Support Program for Chongqing Overseas Returnees (Grant No. cx2021050), the Chongqing Research Program of Basic Research and Frontier Technology, China (Grant No. cstc2021jcyj-msxmX0640), the China Postdoctoral Science Foundation (Grant No. 2021M700612), the Doctor "Through Train" Scientific Research Project of Chongqing (Grant No. CSTB2022BSXM-JCX0087), and the startup funding granted by Chongqing University (Grant No. 0233001104472). We gratefully acknowledge HZWTECH and Hefei Advanced Computing Center for providing computation facilities.

[1] R. A. Kishore, A. Nozariasbmarz, B. Poudel, M. Sanghadasa, and S. Priya, Ultra-high performance wearable thermoelectric coolers with less materials, Nat. Commun. **10**, 1 (2019).

[2] L. E. Bell, Cooling, heating, generating power, and recovering waste heat with thermoelectric systems, Science **321**, 1457 (2008).

[3] J. Mao, G. Chen, and Z. Ren, Thermoelectric cooling materials, Nat. Mater. **20**, 454 (2021).

[4] D. Enescu and E. O. Virjoghe, A review on thermoelectric cooling parameters and performance, Renewable Sustainable Energy Rev. **38**, 903 (2014).

[5] J. Mao, H. Zhu, Z. Ding, Z. Liu, G. A. Gamage, G. Chen, and Z. Ren, High thermoelectric cooling performance of n-type Mg3Bi2-based materials, Science **365**, 495 (2019).

[6] Y. Pei, H. Wang, and G. J. Snyder, Band engineering of thermoelectric materials, Adv. Mater. **24**, 6125 (2012).

[7] K. Biswas, J. He, I. D. Blum, C. I. Wu, T. P. Hogan, D. N. Seidman, V. P. Dravid, and M. G. Kanatzidis, High-performance bulk thermoelectrics with all-scale hierarchical architectures, Nature **489**, 414 (2012).

[8] B. Jiang, Y. Yu, J. Cui, X. Liu, L. Xie, J. Liao, Q. Zhang, Y. Huang, S. Ning, and B. Jia, High-entropy-stabilized chalcogenides with high thermoelectric performance, Science **371**, 830 (2021).

[9] L. Su, D. Wang, S. Wang, B. Qin, Y. Wang, Y. Qin, Y. Jin, C. Chang, and L.-D. Zhao, High thermoelectric performance realized through manipulating layered phonon-electron decoupling, Science **375**, 1385 (2022).

[10] P. Vaqueiro and A. V. Powell, Recent developments in nanostructured materials for high-performance thermoelectrics, J. Mater. Chem. **20**, 9577 (2010).

[11] J. Pei, B. Cai, H.-L. Zhuang, and J.-F. Li, Bi_2Te_3-based applied thermoelectric materials: Research advances and new challenges, Natl. Sci. Rev. **7**, 1856 (2020).

[12] L. D. Hicks and M. S. Dresselhaus, Effect of quantum-well structures on the thermoelectric figure of merit, Phys. Rev. B **47**, 12727 (1993).

[13] G. Mahan and J. Sofo, The best thermoelectric, Proc. Natl. Acad. Sci. **93**, 7436 (1996).

[14] X. Zhang, Y. Guo, Z. Zhou, Y. Li, Y. Chen, and J. Wang, A general strategy for designing two-dimensional high-efficiency layered thermoelectric materials, Energy Environ. Sci. **14**, 4059 (2021).

[15] P. Gorai, E. S. Toberer, and V. Stevanović, Computational identification of promising thermoelectric materials among known quasi-2D binary compounds, J. Mater. Chem. A **4**, 11110 (2016).

[16] W. S. Yun and J. Lee, Single-layer $CdPSe_3$: A promising thermoelectric material persisting in high temperatures, Appl. Phys. Lett. **115**, 193105 (2019).

[17] C. Gong, Y. Zhang, W. Chen, J. Chu, T. Lei, J. Pu, L. Dai, C. Wu, Y. Cheng, and T. Zhai, Electronic and optoelectronic applications based on 2D novel anisotropic transition metal dichalcogenides, Adv. Sci. **4**, 1700231 (2017).

[18] M. R. Burton, T. Liu, J. McGettrick, S. Mehraban, J. Baker, A. Pockett, T. Watson, O. Fenwick, and M. J. Carnie, Thin film tin selenide (SnSe) thermoelectric generators exhibiting ultralow thermal conductivity, Adv. Mater. **30**, 1801357 (2018).

[19] R. Venkatasubramanian, E. Siivola, T. Colpitts, and B. O'quinn, Thin-film thermoelectric devices with high room-temperature figures of merit, Nature **413**, 597 (2001).

[20] C. Niu, H. Wang, N. Mao, B. Huang, Y. Mokrousov, and Y. Dai, Antiferromagnetic Topological Insulator with Nonsymmorphic Protection in Two Dimensions, Phys. Rev. Lett. **124**, 066401 (2020).

[21] I. Errea, M. Calandra, C. Pickard, J. Nelson, R. Needs, Y. Li, H. Liu, Y. Zhang, Y. Ma, and F. Mauri, Quantum hydrogen-bond symmetrization in the superconducting hydrogen sulfide system, Nature **532**, 81 (2016).

[22] J. Hafner, Ab-initio simulations of materials using VASP: Density-functional theory and beyond, J. Comput. Chem. **29**, 2044 (2008).

[23] J. P. Perdew, K. Burke, and M. Ernzerhof, Generalized Gradient Approximation Made Simple, Phys. Rev. Lett. **77**, 3865 (1996).

[24] B. Hammer, L. B. Hansen, and J. K. Nørskov, Improved adsorption energetics within density-functional theory using revised Perdew-Burke-Ernzerhof functionals, Phys. Rev. B **59**, 7413 (1999).

[25] P. Jiang, C. Wang, D. Chen, Z. Zhong, Z. Yuan, Z.-Y. Lu, and W. Ji, Stacking tunable interlayer magnetism in bilayer CrI_3, Phys. Rev. B **99**, 144401 (2019).

[26] V. I. Anisimov, J. Zaanen, and O. K. Andersen, Band theory and Mott insulators: Hubbard *U* instead of Stoner *I*, Phys. Rev. B **44**, 943 (1991).

[27] F. Aryasetiawan, K. Karlsson, O. Jepsen, and U. Schönberger, Calculations of Hubbard *U* from first-principles, Phys. Rev. B **74**, 125106 (2006).

[28] See Supplemental Material at http://link.aps.org/supplemental/10.1103/PhysRevApplied.20.014052 for electronic structures and transport properties of the *A*Mn*X* family.

[29] A. Dascoulidou, P. Müller, and W. Bronger, Ternäre Mangan-Verbindungen AMnX (A = Mg, Ca, Sr oder Ba; X = Si, Ge oder Sn): Neutronenbeugungsuntersuchungen zur Charakterisierung der magnetischen Eigenschaften, Z. Anorg. Allg. Chem. **624**, 124 (1998).

[30] H. J. Zhao, X. Q. Liu, X. M. Chen, and L. Bellaiche, Effects of chemical and hydrostatic pressures on structural, magnetic, and electronic properties of R_2NiMnO_6 (R = rare-earth ion) double perovskites, Phys. Rev. B **90**, 195147 (2014).

[31] C. Xin, B. Song, Z. Sun, Z. Hu, B. Yuan, H. Li, G. Jin, and F. Pan, Intrinsic role of ↑↑↓↓-type magnetic structure on magnetoelectric coupling in Y_2NiMnO_6, Appl. Phys. Lett. **116**, 242901 (2020).

[32] G. K. Madsen and D. J. Singh, BoltzTraP. A code for calculating band-structure dependent quantities, Comput. Phys. Commun. **175**, 67 (2006).

[33] M.-Q. Long, L. Tang, D. Wang, L. Wang, and Z. Shuai, Theoretical predictions of size-dependent carrier mobility and polarity in graphene, J. Am. Chem. Soc. **131**, 17728 (2009).

[34] M. Long, L. Tang, D. Wang, Y. Li, and Z. Shuai, Electronic structure and carrier mobility in graphdiyne sheet and nanoribbons: Theoretical predictions, ACS Nano **5**, 2593 (2011).

[35] J. Chen, J. Xi, D. Wang, and Z. Shuai, Carrier mobility in graphyne should be even larger than that in graphene: A theoretical prediction, J. Phys. Chem. Lett. **4**, 1443 (2013).

[36] S. Basak and M. H. Cohen, Deformation-potential theory for the mobility of excess electrons in liquid argon, Phys. Rev. B **20**, 3404 (1979).

[37] T. Yue, Y. Sun, Y. Zhao, S. Meng, and Z. Dai, Thermoelectric performance in the binary semiconductor compound A_2Se_2 (A = K, Rb) with host-guest structure, Phys. Rev. B **105**, 054305 (2022).

[38] C.-W. Wu, X. Ren, G. Xie, W.-X. Zhou, G. Zhang, and K.-Q. Chen, Enhanced High-Temperature Thermoelectric Performance by Strain Engineering in BiOCl, Phys. Rev. Appl. **18**, 014053 (2022).

[39] J. Taylor, H. Guo, and J. Wang, *Ab initio* modeling of quantum transport properties of molecular electronic devices, Phys. Rev. B **63**, 245407 (2001).

[40] A. Ward, D. Broido, D. A. Stewart, and G. Deinzer, *Ab initio* theory of the lattice thermal conductivity in diamond, Phys. Rev. B **80**, 125203 (2009).

[41] A. Togo and I. Tanaka, First principles phonon calculations in materials science, Scr. Mater. **108**, 1 (2015).

[42] W. Li, J. Carrete, N. A. Katcho, and N. Mingo, ShengBTE: A solver of the Boltzmann transport equation for phonons, Comp. Phys. Commun. **185**, 1747 (2014).

[43] L. Koch, S. Steiner, A.-P. Hoang, A. J. Klomp, K. Albe, and T. Frömling, Revealing the impact of acceptor dopant type on the electrical conductivity of sodium bismuth titanate, Acta Mater. **229**, 117808 (2022).

[44] V. Y. Verchenko and A. A. Tsirlin, Semiconducting and metallic compounds within the $IrIn_3$ structure type: Stability and chemical bonding, Inorg. Chem. **61**, 3274 (2022).

[45] T. Jia, J. Carrete, Z. Feng, S. Guo, Y. Zhang, and G. K. Madsen, Localized dimers drive strong anharmonicity and low lattice thermal conductivity in $ZnSe_2$, Phys. Rev. B **102**, 125204 (2020).

[46] Y. Li, S. Yamamoto, K. Ahmad, Z. Almutairi, K. Koumoto, and C. Wan, Localized vibration and avoided crossing in $SrTi_{11}O_{20}$ for oxide thermoelectrics with intrinsically low thermal conductivity, J. Mater. Chem. A **9**, 11674 (2021).

[47] A. F. Zurhelle, V. L. Deringer, R. P. Stoffel, and R. Dronskowski, Ab initio lattice dynamics and thermochemistry of layered bismuth telluride (Bi_2Te_3), J. Phys.: Condens. Matter **28**, 115401 (2016).

[48] S. Chandra and K. Biswas, Realization of high thermoelectric figure of merit in solution synthesized 2D SnSe nanoplates via Ge alloying, J. Am. Chem. Soc. **141**, 6141 (2019).

[49] Y. Zhou and L. D. Zhao, Promising thermoelectric bulk materials with 2D structures, Adv. Mater. **29**, 1702676 (2017).

[50] L.-D. Zhao, C. Chang, G. Tan, and M. G. Kanatzidis, SnSe: A remarkable new thermoelectric material, Energy Environ. Sci. **9**, 3044 (2016).

[51] X. Qi, W. Ma, X. Zhang, and C. Zhang, Raman characterization and transport properties of morphology-dependent two-dimensional Bi_2Te_3 nanofilms, Appl. Surf. Sci. **457**, 41 (2018).

[52] M. Ahmad, K. Agarwal, N. Kumari, and B. Mehta, KPFM based investigation on the nature of $Sb_2Te_3 : MoS_2$ and Bi_2Te_3: MoS_2 2D interfaces and its effect on the electrical and thermoelectric properties, Appl. Phys. Lett. **111**, 023904 (2017).

[53] C. Chang, M. Wu, D. He, Y. Pei, C.-F. Wu, X. Wu, H. Yu, F. Zhu, K. Wang, and Y. Chen, 3D charge and 2D phonon transports leading to high out-of-plane *ZT* in n-type SnSe crystals, Science **360**, 778 (2018).

[54] Y.-L. Pei, J. He, J. Li, F. Li, Q. Liu, W. Pan, C. Barreteau, D. Berardan, N. Dragoe, and L.-D. Zhao, High thermoelectric performance of oxyselenides: Intrinsically low thermal conductivity of Ca-doped BiCuSeO, NPG Asia Mater. **5**, e47 (2013).

[55] P. Ying, X. Li, Y. Wang, J. Yang, C. Fu, W. Zhang, X. Zhao, and T. Zhu, Hierarchical chemical bonds contributing to the intrinsically low thermal conductivity in α-MgAgSb thermoelectric materials, Adv. Funct. Mater. **27**, 1604145 (2017).

[56] Z. Zhou, X. Yang, H. Fu, R. Wang, X. Lu, G. Wang, and X. Zhou, Anomalous thermal transport driven by electron–phonon coupling in 2D semiconductor h-BP, Adv. Funct. Mater. **32**, 2206974 (2022).

[57] O. Hellman and D. A. Broido, Phonon thermal transport in Bi_2Te_3 from first principles, Phys. Rev. B **90**, 134309 (2014).

[58] L. Lykke, B. B. Iversen, and G. K. H. Madsen, Electronic structure and transport in the low-temperature thermoelectric $CsBi_4Te_6$: Semiclassical transport equations, Phys. Rev. B **73**, 195121 (2006).

[59] Y. S. Hor, A. Richardella, P. Roushan, Y. Xia, J. G. Checkelsky, A. Yazdani, M. Z. Hasan, N. P. Ong, and R. J. Cava, p-type Bi_2Se_3 for topological insulator and low-temperature thermoelectric applications, Phys. Rev. B **79**, 195208 (2009).

[60] F. Jia, Y. Y. Liu, Y. F. Zhang, X. Shu, L. Chen, and L. M. Wu, Bi_8Se_7: Delocalized interlayer π-bond interactions enhancing carrier mobility and thermoelectric performance near room temperature, J. Am. Chem. Soc. **142**, 12536 (2020).

[61] D.-Y. Chung, T. Hogan, P. Brazis, M. Rocci-Lane, C. Kannewurf, M. Bastea, C. Uher, and M. G. Kanatzidis, $CsBi_4Te_6$: A high-performance thermoelectric material for low-temperature applications, Science **287**, 1024 (2000).

[62] H. Jiang, L. Zheng, Z. Liu, and X. Wang, Two-dimensional materials: From mechanical properties to flexible mechanical sensors, InfoMat **2**, 1077 (2019).

[63] J.-W. Jiang, J.-S. Wang, and B. Li, Young's modulus of graphene: A molecular dynamics study, Phys. Rev. B **80**, 113405 (2009).